

Maximum Efficiency and Open-Circuit Voltage of Perovskite Solar Cells

Wolfgang Tress

Abstract This chapter serves as an introduction to the general working principles of solar cells. It starts from the thermodynamics of terrestrial solar cells and fundamentals of semiconductor-based photovoltaics, where the theoretical limits of efficiency and open-circuit voltage as a function of the bandgap are discussed. The chapter describes the prediction of the open-circuit voltage when the photovoltaic action spectra and the electroluminescence quantum efficiency are known. The role of subgap states and several sources of nonradiative recombination, including interfaces to the charge-transport layers, are investigated at open-circuit voltage and fill factor of state-of-the-art perovskite solar cells. Based on these factors, organic–inorganic perovskite solar cells with different architectures and compositions are compared with other solar cell technologies. Low disorder and weak nonradiative recombination are shown to be responsible for the superior performance of mixed cation mixed halide perovskite solar cells, allowing for open-circuit voltages of 1.2 V to be achieved at a bandgap of 1.6 eV.

1 Maximum Power-Conversion Efficiency of a Terrestrial Solar Cell

1.1 Thermodynamics and Black Body Radiation

A solar cell converts energy of light emitted from the sun into electrical energy. The energy flux from the sun is primarily thermal radiation and can be approximated by a black body spectrum at a temperature T_S of ≈ 5800 K outside the earth atmosphere. Prior to reaching the earth's surface, narrow spectral bands have been filtered out by gases in the atmosphere, such as ozone, oxygen, and water vapor (Fig. 1). The spectrum is then called AM X , where X denotes the distance that the

W. Tress (✉)

Laboratory of Photonics and Interfaces (LPI), École polytechnique fédérale de Lausanne (EPFL), 1015, Lausanne, Switzerland
e-mail: wolfgang.tress@epfl.ch

light has traveled through the atmosphere in multiples of its thickness. The standard spectrum for solar cell characterization is AM 1.5 global corresponding to an angle of incidence of $48^\circ = \cos^{-1}(1.5^{-1})$.

Upon absorption of sun light, the absorber's temperature increases to T_A meaning that the energy transferred from the sun heats the absorber "medium". Thus, the solar cell can be treated as a heat engine transforming thermal energy into work in the form of electrical energy. The maximum conversion efficiency of a heat engine is the Carnot efficiency, which considers the conservation of entropy contained in thermal radiation. This entropy ΔS has to be released with a heat flux $\Delta Q = T_0 \Delta S$, with T_0 being the temperature of the surroundings, because electrical energy is entropy-free [1]. Thus, the Carnot efficiency is

$$\eta_C = \frac{T_A - T_0}{T_A} = 1 - \frac{T_0}{T_A}. \quad (1)$$

In order to obtain the maximum Carnot efficiency, the temperature difference between the medium and the surroundings should be maximized to avoid a large heat flux associated with the conservation of entropy. As the temperature of the surroundings is fixed, the medium should be as hot as possible.

Coming back to the energy source, we notice that the heat is transferred from the sun to the medium by radiation. In the optimum case, the medium itself is capable of absorbing all the incident radiation. Thus, it is a black body as well, which according to Kirchhoff's law reemits part of the absorbed photon flux. Spectrum

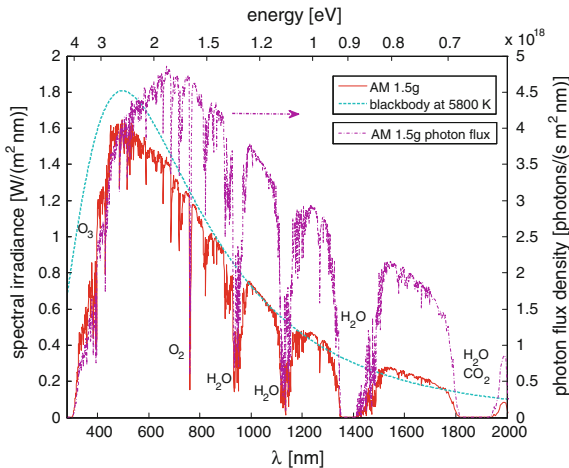


Fig. 1 The standard solar spectrum, AM1.5 g, used for solar cell characterization. The irradiance integrated over wavelength results in 100 mW cm^{-2} . The spectral shape can be approximated with a black body radiator at 5800 K. The gaps are due to absorption of compounds in the atmosphere (O_3 , O_2 , H_2O , ...). Dash-dotted is the corresponding photon flux, obtained when dividing the irradiance spectrum (red) by the photon energy at each wavelength

$B(\lambda, T)$ and emitted power per surface area (I) are described by Planck's and the Stefan–Boltzmann law, respectively:

$$B(\lambda, T) = \frac{2hc^2}{\lambda^5} \frac{1}{\exp \frac{hc}{\lambda k_B T} - 1}, \quad (2a)$$

$$I = \sigma T^4, \quad (2b)$$

with wavelength λ , Planck's constant h , speed of light c , Boltzmann constant k_B , and Stefan–Boltzmann constant σ . Thus, the higher T_A , the more intense the emission. If work is not extracted from the absorber medium, it reaches equilibrium with the sun and the surroundings. For a maximum concentration of the sun light, i.e., a situation where all the emitted flux from the absorber medium is redirected toward the sun, the medium would reach the temperature of the sun (surface) T_S and emit the solar spectrum back to the sun. However, in this situation work cannot be extracted. This requires a lower temperature of the absorber medium, and the fraction of extractable energy can be written as the difference between absorbed and emitted energy flux according to the Stefan–Boltzmann law:

$$\eta_{\text{rad}} = \frac{\sigma(T_S^4 - T_A^4)}{\sigma T_S^4} = 1 - \frac{T_A^4}{T_S^4}. \quad (3)$$

This equation demands for a low T_A , which is in contrast to the requirements for obtaining a high Carnot efficiency. Consequently, the highest solar to work conversion efficiency is reached at a T_A such that $T_0 < T_A < T_S$. The optimum T_A is 2478 K with a corresponding $\eta_{\text{max}} = \eta_{\text{rad}}\eta_C$ of 85 %. For a conversion of, e.g., mechanical work of the heat engine into electricity, we can imagine a generator with almost 100 % power-conversion efficiency. Consequently, the highest power-conversion efficiency of a terrestrial solar cell might approach but cannot exceed 85 %.

In case of a nonconcentrated system, the thermodynamic limit is reduced as the medium will emit into a larger solid angle and thus increase the entropy. The solid angle of the sun seen from the earth is 6.8×10^{-5} (resulting from the long distance between the earth and the sun and the sun's diameter), which is a factor 46,200 smaller than the solid angle of emission into a hemisphere [1, 2]. This factor should be considered in the emitted intensity in Eq. 3 and reduces η_{max} to only a few percent. Thus, efficient solar–thermal energy conversion using a heat engine requires concentration of sun light. This is not necessarily the case for photovoltaic systems using bandedge absorbers as we will see in the following sections. They can operate efficiently at low concentrations of the sun light and at ambient temperatures. Nevertheless, every solar-based energy converter, independent of its implementation, is tied to the 85 % limit.

1.2 Semiconductor-Based Photovoltaics

A semiconductor is characterized by a bandgap E_g making its optical properties differ from those of a black body. In an ideal semiconductor, only photons with energy higher than E_g are absorbed by promoting an electron from the valence to the conduction band and leaving a hole in the valence band (Fig. 2). Thus, the onset of the absorption spectrum is at the energy of the bandgap. Incident photons with lower energies are transmitted. The peak energy of the emitted photon spectrum is located close to the bandgap energy as well and almost independent of temperature in contrast to the black body radiation. Mainly the spectral width increases with temperature due to an increased thermal energy of electrons and holes in their respective bands. To be distinguished from thermal (i.e., black body) radiation, this kind of narrow radiation is called luminescence.

To harvest as many solar photons as possible, the bandgap of the semiconductor should be minimized (Fig. 1), which allows for the highest electron-hole generation rate, and we can write the below equation for the photocurrent:

$$J_{\text{ph,ideal}} = e \int_{E_g}^{\infty} \Phi_{\text{AM1.5g}}(E) dE \quad (4)$$

with $\Phi_{\text{AM1.5g}}$ describing the spectral photon flux, i.e., the number of photons per area, time, and energy (or wavelength) interval. To generate a net electrical current in an external circuit, electrons and holes have to be extracted at two different contacts. For the moment, we only introduce the concept of so-called charge-selective contacts: an electron-selective contact would only allow electrons to pass and reject holes, and vice versa for a hole-selective contact. We will come to implementations of such selective contacts later.

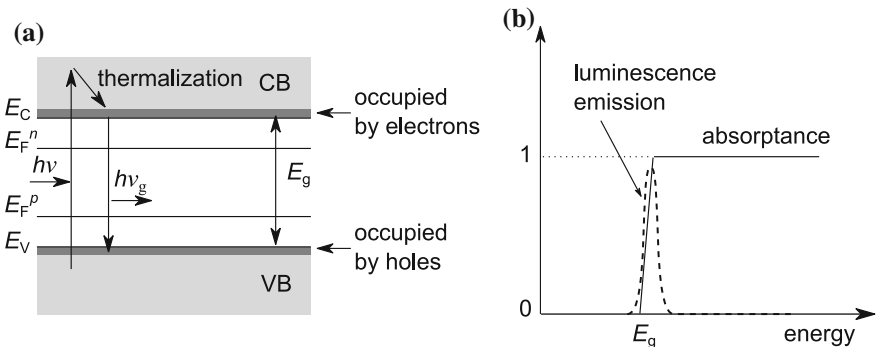


Fig. 2 Optoelectronic basics of semiconductors **a** Sketch of band diagram with bandgap E_g , conduction and valence band edge E_C and E_V , respectively, and quasi-Fermi levels for electrons E_F^n and holes E_F^p , which are split due to illumination. **b** Schematics of ideal absorbance and emission

However, a large photocurrent is not sufficient: the relevant parameter is the electrical power of the extracted charge flux. This power is the product of flux and the (average) free energy of one extracted electron-hole pair, which is proportional to the voltage measurable externally. Thus, we need an expression for this energy, which is mainly electrochemical in nature and depends on the electrical potential energy as well as the concentration of charges (chemical energy). We expect the potential energy of the electron-hole pair to scale with the bandgap, consistent with the fact that the peak of luminescence radiation is located at the bandgap energy. This holds even for absorbed photons with much higher energy, which create an electron (hole) that is located much higher (deeper) in the conduction (valence) band compared to the band edges. However, this electron relaxes quickly (ps) to the band edge due to energy transfer to phonons (Fig. 2a), analogously to Kasha's rule in the photochemistry of electronically excited molecules. The excess energy is lost as heat and the average energy of the electron remains at $E_C + \frac{3}{2}k_B T$. This fast process assisted by phonons is called thermalization. Consequently, the higher the bandgap, the lower are the overall thermalization losses, when absorbing a broad spectrum such as AM1.5 g. Therefore, when tuning the bandgap to reach high efficiency, there is a tradeoff between harvesting as many photons as possible and maximizing the energy of extracted charges.

To determine the optimum bandgap, we need to find an expression for the electrical energy of an extracted electron-hole pair. Coming back to the previous section on thermodynamics, we know that electrical energy is an entropy-free part of the energy. Thus, we need to know the entropy of an electron (hole) in the electron (hole) gas in the conduction (valence) band. After longer derivation [1] it is found that the entropy-free part of the energy, i.e., the electrochemical potential η_e of an electron in the conduction band, is:

$$\eta_e = E_C - k_B T \ln \frac{N_C}{n}, \quad (5)$$

where n is the electron density (number of electrons per unit volume) and N_C is the effective density of states, i.e., a parameter that represents the amount of available states close to the band edge. The second term increases linearly with temperature as expected for an energy flux related to entropy ($\Delta Q = T\Delta S$). ΔQ becomes 0 either at $T \rightarrow 0$ K or when the density of states is completely filled ($n = N_C$), i.e., there is only one microscopic state possible without any permutations (although in this case, this equation does not hold any more as it contains approximations valid for low n only) [2]. Analogously, we obtain for (positively charged) holes p :

$$-\eta_h = E_V + k_B T \ln \frac{N_V}{p}. \quad (6)$$

In steady state, one electron is extracted together with one hole to conserve charge and obey a continuity equation for electrons. The total energy is then the sum of the electrochemical potentials

$$eV = \eta_e + \eta_h = E_C - E_V - k_B T \ln \frac{N_C N_V}{np} = E_g - k_B T \ln \frac{N_C N_V}{np}. \quad (7)$$

Here, we introduce the externally measurable voltage V , which is expressed as the energy of one extractable electron-hole pair in the electron gas divided by the elementary charge e . This equation shows that the idea of a large bandgap required to maximize the energy of an extracted electron-hole pair is correct.

From Eqs. 5 and 6, we recognize that the electrochemical potentials are the quasi-Fermi energies:

$$n = N_C \exp\left(-\frac{E_C - E_F^n}{k_B T}\right) \rightarrow E_F^n = \eta_e \quad (8a)$$

$$p = N_V \exp\left(-\frac{E_F^p - E_V}{k_B T}\right) \rightarrow E_F^p = -\eta_h \quad (8b)$$

As electrons are fermions, their concentration is determined by Fermi Dirac statistics. The Fermi level E_F is defined as the energy at which the probability of finding the fermion is $1/2$. In a metal E_F describes the highest energy for electrons in the bands at $T \rightarrow 0$ K.

To obtain the electron density in general, the statistics is multiplied by the energetic distribution of available states (so-called density of states, DOS). For electrons in the conduction band (CB) we get

$$\begin{aligned} n &= \int_{\text{CB}} f(E) \times \text{DOS}_{\text{CB}}(E) dE = \int_{\text{CB}} \frac{1}{1 + \exp\left(\frac{E - E_F}{k_B T}\right)} \times \text{DOS}_{\text{CB}}(E) dE \\ &\approx \int_{\text{CB}} \exp\left(-\frac{E - E_F}{k_B T}\right) \times \text{DOS}_{\text{CB}}(E) dE \end{aligned} \quad (9)$$

This approach results in the previous equations considering a certain DOS and the Boltzmann approximation. Under equilibrium, i.e., no voltage applied or generated by light, we obtain

$$E_F^n = E_F^p \quad (10)$$

and

$$np = n_i^2 = N_C N_V \exp\left(-\frac{E_g}{k_B T}\right), \quad (11)$$

with the intrinsic (i.e., thermally generated) charge carrier density n_i . The definition of quasi-Fermi levels under illumination or applied voltage (nonequilibrium) is possible as thermalization within a band is commonly much faster than a spontaneous transition of an electron from conduction to valence band (i.e., electron-hole

recombination). Thus, electrons and holes are in equilibrium within their respective band but not amongst each other. This situation can be called quasiequilibrium, described by two separate Fermi distributions for electrons and holes.

In Eq. 7 the electrochemical energy of the extracted electron-hole pair is not solely determined by the bandgap, but also contains a term that depends on electron and hole concentrations (chemical energy). In a solar cell under illumination, the concentration of charges is built-up by the absorption of light (the so-called charge carrier generation G), but it cannot reach infinitely large numbers as the competing process of recombination sets in. The rate of band-to-band recombination of an electron with a hole can be expressed as

$$R = \beta np. \quad (12)$$

Intuitively we can say that the recombination rate R scales with the probability of an electron finding a hole. In steady state at open circuit under a given light intensity $\propto G$, all charges recombine, i.e., $R = G$ and therefore the open-circuit voltage is (Eq. 12 in Eq. 7):

$$eV_{oc} = E_g - k_B T \ln \frac{N_C N_V \beta}{G}. \quad (13)$$

This equation describes V_{oc} as a function of temperature, light intensity (which is $\propto G$), and bandgap. An expression for the radiative recombination constant β will be derived subsequently.

1.3 Radiative Limit of the Open-Circuit Voltage

We want to start from the equilibrium situation and extend it to the operation points of the solar cell. Here, equilibrium means that the semiconductor is in the dark without any applied bias. In this case, “dark” describes a surrounding at a temperature $T_0 = 300$ K. This temperature gives rise to a background radiation with a black body spectrum at T_0 according to Planck’s law

$$\Phi_{BB}(E) = \frac{1}{4\pi^2 \hbar^3 c^2} \frac{E^2}{\exp\left(\frac{E}{k_B T_0}\right) - 1}. \quad (14)$$

This equation is identical to Eq. 2a, but expressed in terms of a photon flux as a function of energy (instead of intensity as a function of wavelength). The semiconductor absorbs part of this spectrum and has to emit the same part because it is in equilibrium with the surrounding

$$\Phi_{\text{abs},0} = \int a(E)\Phi_{\text{BB}}(E)dE = \Phi_{\text{em},0}. \quad (15)$$

Here, $a(E)$ is the absorbance (0...1), where we could use a Heaviside step function switching from 0 to 1 at E_g for an ideal semiconductor as we did in Eq. 4.

This equality is true not only for the absolute flux, but also for each energy (or wavelength) according to the principle of ‘‘detailed balance’’:

$$\Phi_{\text{em},0}(E) = a(E)\Phi_{\text{BB}}(E). \quad (16)$$

It means that the emission spectrum $\Phi_{\text{em}}(E)$ can be predicted when absorption coefficient and temperature are known [3].

To experimentally determine the emission spectrum, we consider the nonequilibrium case: Additional electrons and holes need to be generated in the semiconductor, either by light or by applying a voltage and injecting charges. The former option results in photoluminescence, and the latter in electroluminescence. We verify the applicability of the detailed balance theory for a $\text{CH}_3\text{NH}_3\text{PbI}_3$ perovskite solar cell. Rather than using the absorption spectrum, we use the photocurrent action spectrum (external quantum efficiency EQE_{PV}), which ideally is proportional to the absorption spectrum and easier to obtain experimentally. Based on an extended version of the reciprocity between absorption, emission, and electronic charge transport, $a(E)$ can be interchanged with $\text{EQE}_{\text{PV}}(E)$ [4]. A measured EQE_{PV} onset is shown in Fig. 3a. By multiplying the $\text{EQE}_{\text{PV}}(E)$ with $\Phi_{\text{BB}}(E)$, shown as dashed line for $T_0 = 320$ K, we calculate an emission spectrum (Fig. 3b), which fits the measured electroluminescence spectrum very well. This indicates that the assumption of an unmodified spectrum even under illumination or applied voltage is justified. Coming back to Eq. 12, we can write in equilibrium:

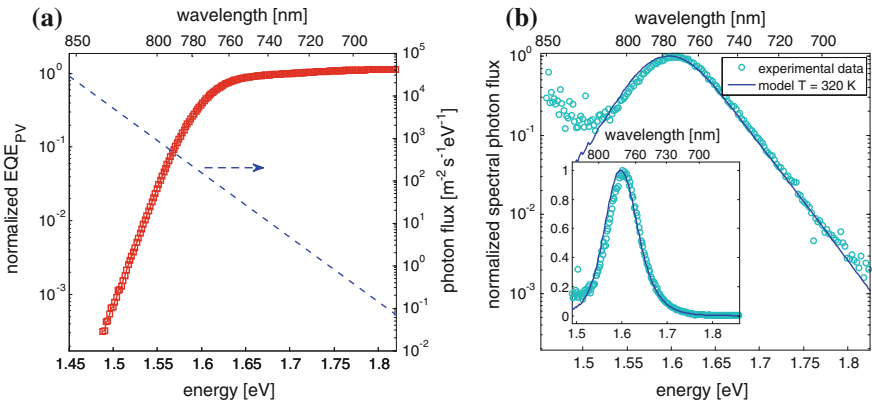


Fig. 3 Bandedge of $\text{CH}_3\text{NH}_3\text{PbI}_3$ **a** Spectral photocurrent onset in terms of the external quantum efficiency of a solar cell (*solid line*) and black body photon flux at 320 K (*dashed*). **b** Measured and calculated electroluminescence emission. Data originally published in Ref. [6]

$$G_0 = \int \alpha(E) \Phi_{\text{BB}}(E) dE = \beta n_0 p_0 = \beta n_i^2. \quad (17)$$

Thus, the radiative recombination constant β can be calculated knowing the intrinsic charge carrier density n_i (Eq. 11) and the absorption coefficient $\alpha(E)$. Assuming parabolic band minima (DOS) with an effective electron (hole) mass $m^* = 0.228$ (0.293) m_0 (m_0 is the electron rest mass) [5], we can derive $N_{\text{C,V}}$ using Eq. 9 ($\rightarrow N_{\text{C,V}} = 2 \left(\frac{2\pi m^* k_B T}{h^2} \right)^{\frac{3}{2}}$, derivation not shown), and in turn n_i (Eq. 11). With Eq. 17 we obtain the value of $\beta \approx 10^{-11} \text{cm}^3 \text{s}^{-1}$.

Under bias (or illumination), n and p become larger than n_i and the common Fermi level (Eq. 10) splits into separate (quasi) Fermi levels for electrons and holes according to Eq. 8a, 8b, leading to $np = n_i^2 \exp \frac{E_e^q - E_h^q}{k_B T}$.

Thus, recognizing that eV is the difference between the quasi-Fermi levels at the contacts, the enhanced recombination gives rise to an emitted photon flux Φ_{em} exponentially increasing with the applied voltage:

$$\Phi_{\text{em}} = \Phi_{\text{em},0} \exp \frac{eV}{k_B T}. \quad (18)$$

If we think of the device operated as a light-emitting diode, Φ_{em} is achieved at a particular electric current injected into the device:

$$J_{\text{rad}} = e \left(\Phi_{\text{em},0} \exp \frac{eV}{k_B T} - \Phi_{\text{em},0} \right) = e \Phi_{\text{em},0} \left(\exp \frac{eV}{k_B T} - 1 \right). \quad (19)$$

We recognize that this equation is identical to the Shockley diode equation when the saturation current is set as $J_0 = e \Phi_{\text{em},0}$.

If the device is operated as a solar cell under illumination, the photocurrent J_{ph} should be added to Eq. 19:

$$J_{\text{ideal}} = e \Phi_{\text{em},0} \left(\exp \frac{eV}{k_B T} - 1 \right) - J_{\text{ph}}. \quad (20)$$

Now, we can write an equation for the open-circuit voltage, setting J_{ideal} to 0:

$$V_{\text{oc,rad}} = \frac{k_B T}{e} \ln \left(\frac{J_{\text{ph}}}{e \Phi_{\text{em},0}} + 1 \right). \quad (21)$$

This is the ideal V_{oc} of a solar cell if only radiative recombination is present. For $\text{CH}_3\text{NH}_3\text{PbI}_3$ perovskite solar cells, we calculate a value of 1.33 V [6, 7]. Variations in bandgap as a function of film morphology can slightly (by $\approx \pm 0.02\text{V}$) alter this value. As we will discuss later, (partially) substituting atoms/ions on the perovskite lattice is a strategy to modify the bandgap.

1.4 Shockley–Queisser Limit

Since current is not extracted at V_{oc} , and the power is the product of current and voltage, the power at open circuit is 0. Instead, it is largest at the so-called maximum power point (MPP), which is found by searching for the maximum of $J \times V$. For $\text{CH}_3\text{NH}_3\text{PbI}_3$ perovskite with a bandgap of $\approx 1.55\text{--}1.6$ eV, the maximum efficiency would be 31–30 %. The ideal current-voltage curve according to Eq. 20 is visualized in Fig. 4a, including the extractable power. The fill factor is defined as $\text{FF} = \frac{J_{\text{MPP}} V_{\text{MPP}}}{J_{\text{sc}} V_{\text{oc}}} = \frac{\eta I_{\text{light}}}{J_{\text{sc}} V_{\text{oc}}}$ with the short-circuit current density $J_{\text{sc}} = J_{\text{ph}}$ and the incident light intensity I_{light} . Figure 4b shows the maximum J_{SC} as a function of the bandgap calculated using Eq. 4 with varied E_g . For an E_g of 1.6 eV, we expect a theoretical photocurrent of 25 mA cm^{-2} , which does not include any optical or electrical losses that reduce this value by $1\text{--}3 \text{ mA cm}^{-2}$ for the best perovskite solar cells [8, 9]. The resulting power-conversion efficiency (Shockley–Queisser, SQ limit [10]) as a function of the bandgap is shown in Fig. 4c, where an E_g between 1.1 and 1.4 eV allows an efficiency of ≈ 33 %. The decrease of η for larger E_g is due to transmission losses and thus low photon harvesting (low J_{SC} , cf. Fig. 4b). For reduced E_g , the voltage is low and most of the energy is lost due to thermalization.

The losses discussed so far are unavoidable. However, in implementations of solar cells, additional losses occur, which will be discussed in the following sections of this chapter. The circles in Fig. 4c show how closely solar cells based on different semiconductor material with different E_g approach their theoretical radiative limit. Solar cells based on the direct semiconductor GaAs reach an efficiency >28 % coming very close to their theoretical limit. Photovoltaic devices based on silicon, the most common commercial material, show additional losses, but have an efficiency still exceeding 25 %. Perovskite and CIGS solar cells exhibit similar performance, where today’s best perovskite solar cell is already closer to the Shockley–Queisser limit than the best CIGS cell.

2 The Bandgap

2.1 Absorption Onset and Subgap Urbach Tail

The SQ limit was calculated for a step function in absorption. However, as shown in Fig. 3a, the absorption is not a Heaviside function but contains a contribution below E_g . This is detrimental, because these subgap states hardly contribute to photocurrent. However, they do participate in recombination entering Eq. 15 enhanced by a multiplication with $\Phi_{\text{BB}}(E)$. Thus, a steep absorption onset is preferred. It should follow at least $\exp\left(\frac{E}{k_{\text{B}} T_0}\right)$ to compensate for the exponential increase of $\Phi_{\text{BB}}(E)$ with decreasing energy. Figure 5 shows the absorption onset of $\text{CH}_3\text{NH}_3\text{PbI}_3$ perovskite in comparison with other solar cell materials [12]. Due to

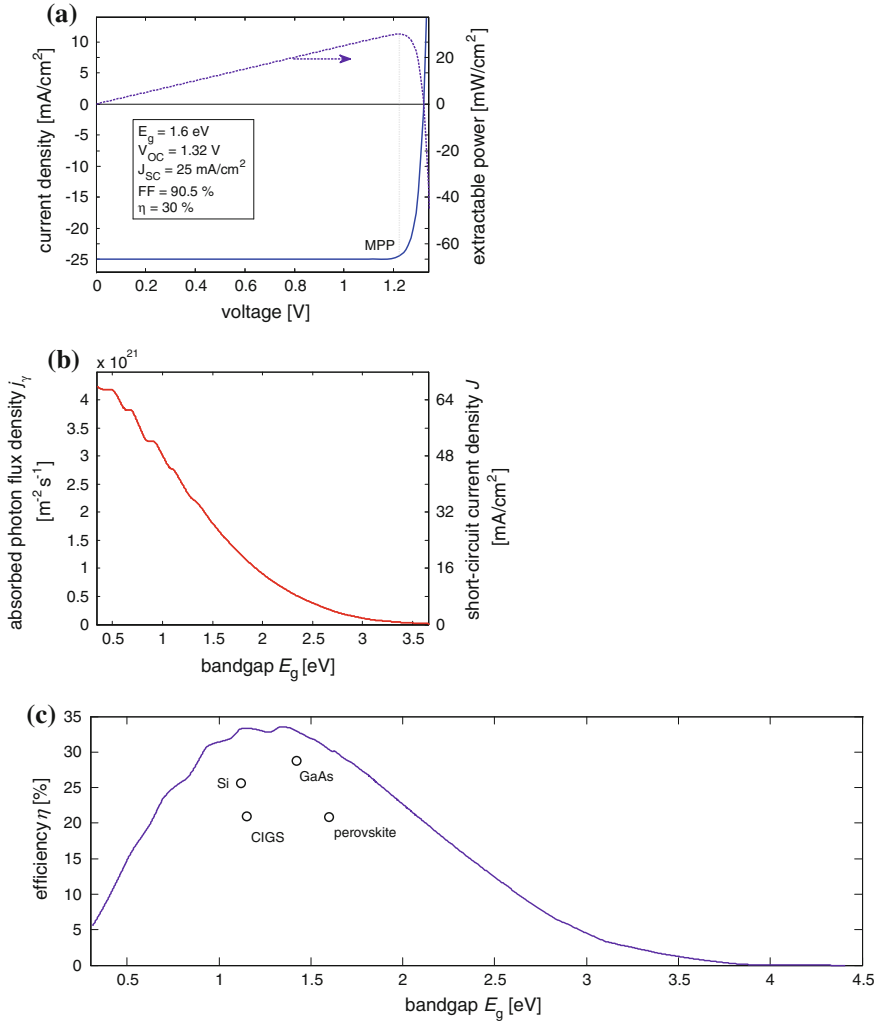
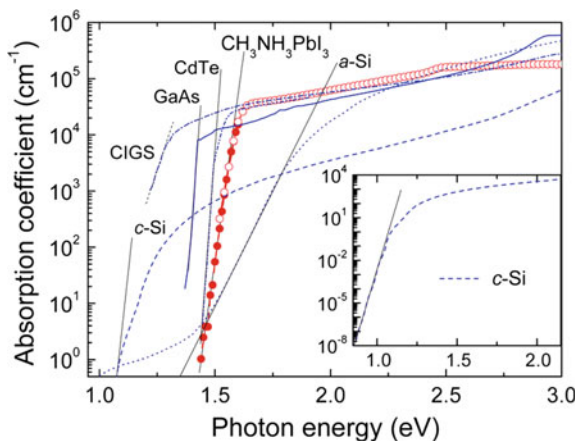


Fig. 4 Shockley–Queisser limit **a** Theoretical J - V curve and power output for an ideal semiconductor with a bandgap of 1.6 eV. **b** Harvested photon flux and short-circuit current density as a function of the bandgap. **c** Maximum power-conversion efficiency as a function of bandgap and record values [9, 11] experimentally achieved so far

its direct bandgap the absorption coefficient above bandgap is similar to the one of GaAs and much steeper than in crystalline or amorphous Si. Additionally, the distribution of subgap states is narrow.

The absorption coefficient below the bandgap shows a so-called Urbach tail. Its origin is from various sources of disorder that generate exponentially decaying densities of states below the conduction and above the valence band. Those could be impurities, ionic positional disorder, vibrational fluctuations of atoms, etc. Their

Fig. 5 Absorption coefficient of different solar cell materials. The *black lines* denote an exponential fit to the Urbach tail. Reprinted with permission from [12]. Copyright 2014 American Chemical Society



common feature is that they locally perturb the periodic crystal potential giving rise to fluctuations of the potential that electrons close to the band edges see. The steep rise and resulting low Urbach energy indicates that the disorder in the $\text{CH}_3\text{NH}_3\text{PbI}_3$ perovskite is low due to its high (nano-) crystallinity. In general, the absorption onset of nano-crystalline perovskite depends on the morphology of the film, mainly on the crystallite size. It shifts toward larger energies with smaller crystallites, possibly due to strain in the material [13].

2.2 Tuning of the Bandgap and Tandem Devices

Until now we have discussed the $\text{CH}_3\text{NH}_3\text{PbI}_3$ perovskite with a bandgap of 1.55 to 1.6 eV. Similar to other compound semiconductors, a partial replacement of components with others of the same ionic charge and fitting into the lattice (Goldschmidt tolerance factor) facilitates tuning of the bandgap of the perovskite. Here, the organic cation has only minor influence, as it is not directly contributing to the valence and conduction band but changing lattice parameters. Replacing methylammonium (CH_3NH_3) by the bigger formamidinium ($\text{HC}(\text{NH}_2)_2$) results in a decrease of E_g (by ≈ 50 meV), slightly shifting the maximum η toward its optimum [14–17]. Using the smaller Cs instead increases the bandgap by ≈ 100 meV [14, 17]. This trend follows the tight-binding model of more closely spaced atoms having more interaction, and thus stronger splitting of their states into broader bands which in turn results in a more narrow bandgap. In case of the perovskite, size effects controlling the metal–halide–metal bond angles [18] are accompanied with further effects such as modified hydrogen bonding and spin orbit coupling when interchanging the monovalent (organic) cation [19]. Note that due to the antibonding nature of the valence states, the bandgap shows an anomalous decrease with temperature [20].

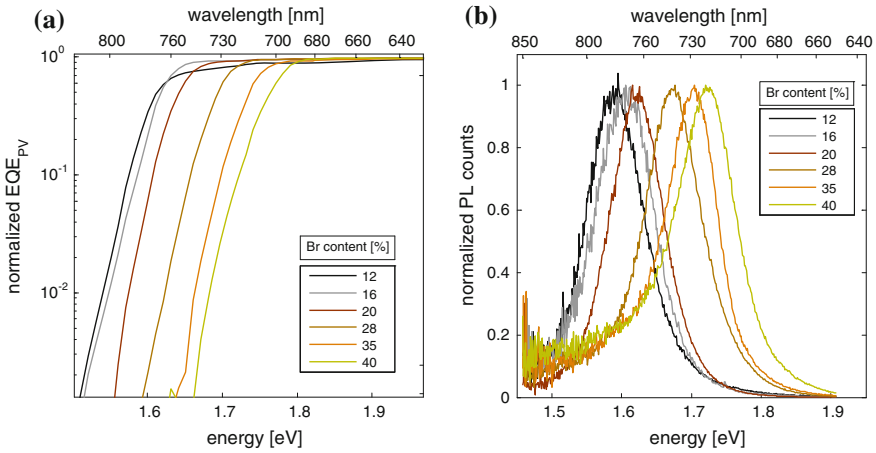


Fig. 6 Mixed MA-FA perovskites with mixed halides **a** The photocurrent onset as a function of the molar Br content, not showing any considerable changes in the Urbach energy. **b** Photoluminescence spectra confirming a shift of the bandgap. The signal at 1.5–1.6 eV might be due to some iodine rich phases in the samples with larger bromine content

More influential are replacements of the halide itself using, e.g., Br [17, 21]. Figure 6 shows photocurrent response (EQE_{PV}) and PL spectra for perovskites with different I:Br molar ratios in the precursor solutions. (These compounds contain a mixture for the organic cation as well because formamidinium-iodide is added to the precursor solution). The data shows that E_g increases monotonically upon increasing substitution of I with Br (similar to highly efficient Cs $\text{HC}(\text{NH}_2)_2$ mixed systems [22]). At the same time, the Urbach tail is maintained at low energies of approx. 15 meV. Calculating the maximum V_{oc} using Eq. 21, we get an increase of $V_{\text{oc,rad}}$ from 1.33 to 1.47 V, when the Br content reaches 40 %. However, the maximum η would decrease from 30 to 27 %. Thus, for a single junction solar cell, there is no reason for increasing E_g except that a higher voltage is preferred to a higher current due to practical reasons such as reduction of resistive losses.

However, tuning the bandgap becomes important when making multijunction solar cells, where several solar cells are stacked on top of each other with the solar cell with the largest E_g employed as the front cell. This approach is a strategy to overcome the Shockley–Queisser limit, as thermalization losses are reduced by collecting the high energy photons at higher voltage. The ideal combination for a two-junction (tandem) solar cell would yield a maximum η of > 42 % with $E_{g1} = 1.0$ eV and $E_{g2} = 1.9$ eV [23]. Technologically interesting is a combination of perovskite with silicon [24–26]. For a monolithic integration the photocurrent should be matched, meaning that Si, which delivers a maximum current of almost 42 mA cm^{-2} , should be combined with a perovskite solar cell providing 21 mA cm^{-2} . Ideally, this current could be achieved using a mixed halide perovskite with a bandgap of 1.75 eV. Then, half of the incident photon flux is converted into charges that are collected at a larger voltage compared to the voltage

obtainable with silicon. This boosts the theoretical efficiency from 33 to >40 %. Using realistic values including optical and electrical losses for Si and perovskite solar cell, efficiencies of around 30 % are expected to be feasible in a tandem configuration [27, 28].

3 Nonradiative Recombination

3.1 Quantum Efficiency of Electroluminescence

So far, the solar cell was treated as ideal, which means that only theoretically unavoidable loss processes have been considered. Regarding recombination, this is radiative recombination only. In that case, the solar cell operates at its radiative limit. However, in reality nonradiative losses are present in addition, reducing charge carrier densities in Eq. 7 and consequently the V_{oc} .

Coming back to the derivation of V_{oc} based on detailed balance (Eq. 19), we consider a quantum efficiency of emission for the injection current:

$$J_{rad}(V) = EQE_{EL} J_{inj}(V). \quad (22)$$

EQE_{EL} is the external quantum efficiency of electroluminescence. We can expand the equation for V_{oc} (Eq. 21) to

$$V_{oc} = \frac{k_B T}{e} \ln \left(EQE_{EL} \frac{J_{ph}}{e \Phi_{em,0}} + 1 \right) \approx V_{oc,rad} - \frac{k_B T}{e} \ln EQE_{EL}. \quad (23)$$

Thus, a reduction of the EQE_{EL} by a factor of 10 is equivalent to a decrease of V_{oc} by $\frac{k_B T}{e} \ln 10 = 60$ mV at room temperature. The EQE_{EL} should be determined at V_{oc} . Practically, it is measured in the dark by driving the solar cell as an LED, detecting the emitted photon flux and dividing it by the injected electron flux.

Knowing EQE_{EL} and EQE_{PV} , which is required to calculate J_{ph} and $e \Phi_{em,0}$ (Eqs. 4 and 15):

$$J_{ph} = e \int EQE_{PV}(E) \Phi_{AM1.5g}(E) dE; e \Phi_{em,0} = e \int EQE_{PV}(E) \Phi_{BB}(E) dE, \quad (24)$$

we can predict the real V_{oc} of a given solar cell [4, 29]. Differences in V_{oc} for different experimental implementations of a solar cell with the same semiconductor are mainly caused by variations of the nonradiative loss that decrease EQE_{EL} . These changes explain the differences observed in V_{oc} for perovskite solar cells, which are reported between 0.7 and 1.2 V, whereas $V_{oc,rad} \approx 1.33$ V is a material property. Table 1 shows examples for perovskite fabricated by different methods and employed in different device architectures [6, 9]. Avoiding a hole transport layer decreases EQE_{EL} .

Table 1 Measured J_{sc} and V_{oc} compared to calculated values based on measured EQE_{PV} and EQE_{EL}

		J_{sc} [mA cm ⁻²]	$V_{oc, \text{measured}}$ [V]	$e\Phi_{em,0}$ [mA cm ⁻²]	$V_{oc, \text{rad}}$ [V]	EQE_{EL} at $J_{inj} = J_{sc}$	nonrad. loss [V]	$V_{oc, \text{calc}}$ [V]
Two-step 2014	TiO ₂	20	1.01	9×10^{-22}	1.33	4×10^{-6}	0.32	1.01
	Al ₂ O ₃	19	1.02	10^{-21}	1.32	3×10^{-5}	0.27	1.05
	No HTL	11	0.77	3×10^{-22}	1.34	2×10^{-9}	0.52	0.82
One-step 2016		20	1.18^a	$\approx 10^{-21}$	1.33	3×10^{-3a}	0.15	1.18

^anonstabilized

The perovskite in the two-step method is CH₃NH₃PbI₃, [6, 30] whereas it is a mixed cation mixed halide perovskite in the one-step device [9]

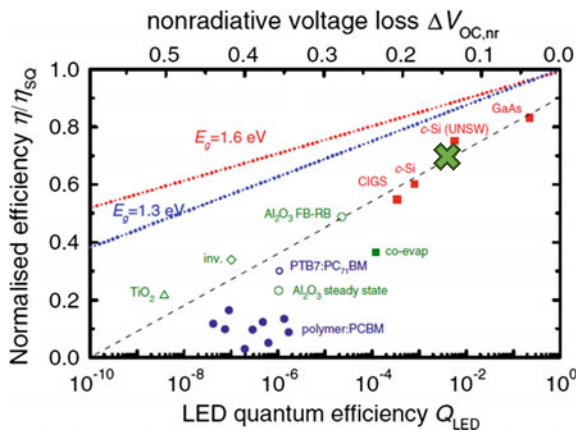


Fig. 7 Power-conversion efficiency for different solar cell technologies normalized to the Shockley-Queisser limits as a function of EQE_{EL} (here denoted as Q_{LED}), equivalent to the nonradiative V_{oc} loss of $\Delta V_{oc,nr} = -26 \text{ mV} \times \ln EQE_{EL}$ (top axis). The dotted lines define the theoretical limits of various EQE_{EL} at the denoted bandgaps. Different CH₃NH₃PbI₃ perovskite fabrication technologies are shown in green. The green cross marks the most efficient perovskite solar cell. Different organic solar cells are shown in blue. The dashed line is a guide to the eye representing the approximate experimental trend. Reprinted and modified with permission from [31]. Copyright 2015 by the American Physical Society

due to surface recombination. On the other hand, employing hole transport layer and tuning the morphology increases EQE_{EL} and thus the measured V_{oc} .

Figure 7 compares the record value of EQE_{EL} for perovskite solar cells [9] (marked with a green cross) with other technologies [31]. The direct semiconductor GaAs yields the highest values due to a high internal luminescence yield. In silicon, EQE_{EL} is limited by Auger and surface recombination [32, 33]. The trend line (dashed) visualizes that in experiment the factor determining the efficiency is EQE_{EL} defining how closely V_{oc} approaches $V_{oc,rad}$.

3.2 Identifying Recombination Mechanisms

The exact source of nonradiative recombination in perovskites has not yet been identified. In addition to recombination at the contacts, defect recombination in the material itself plays a role. Defects might originate from impurities, grain boundaries, or additional crystalline/amorphous phases, e.g., resulting from unreacted precursors. Furthermore, intrinsic defects due to dislocations, interstitials, vacancies, or antisites might give rise to electronically active states. Theoretical studies on whether these defects are active as recombination centers yielded rather contradictory results [34–37].

Shockley-Read-Hall (SRH) theory [38] describes recombination through defects states:

$$R = \frac{np - n_i^2}{\tau_p(n + n_1) + \tau_n(p + p_1)} \quad (25)$$

with $n_1 = N_C \exp\left(-\frac{E_C - E_T}{k_B T}\right)$, $p_1 = N_V \exp\left(-\frac{E_T - E_V}{k_B T}\right)$, and lifetimes for electrons and holes $\tau_{n,p}$. E_T is the energy of the trap. For multiple traps or for a distribution in energy, the right-hand side of Eq. 25 is a sum over all E_T . Investigating Eq. 25, we find that midgap traps ($E_C - E_T \approx E_T - E_V$) are most active as recombination centers. This is in line with the intuitive explanation that midgap traps allow for equally efficient electron and hole capture. Assuming that most of the present charge carriers are photogenerated, thus $n \gg n_1$ and $n \gg n_i$, and considering one dominating SRH lifetime τ , we can approximate R :

$$R \propto \frac{n}{\tau}. \quad (26)$$

Following the same procedure as for direct recombination in Eqs. 11 and 12, we express V_{oc} as a function of light intensity in case of SRH recombination

$$eV_{oc} = E_g - 2k_B T \ln \frac{\sqrt{N_C N_V} \tau}{G}. \quad (27)$$

In general, we can write for the slope of V_{oc} versus $\log_{10} G/(1\text{m}^{-3}\text{s}^{-1})$: $n_{ID} k_B T \ln 10$, where $n_{ID} = 1$ for radiative recombination and $n_{ID} = 2$ for SRH recombination. The parameter n_{ID} is called the ideality factor and lies between 1 and 2, if both recombination processes are present. It is introduced for the dark J - V curve (cf. Eq. 9) as well:

$$J_{inj} = J_0 \left(\exp \frac{eV}{n_{ID} k_B T} - 1 \right). \quad (28)$$

Figure 8a shows the J - V curve of a perovskite solar cell in the dark (blue). It is governed by shunt and series resistances for voltages <0.8 and >1.2 V, respectively. The exponential increase of J between the resistance limited regions is described by Eq. 28, where $n_{ID} = 2$. Consequently, the dominant recombination mechanism is of SRH type. The red curve shows the emitted photon flux with an exponential rise in the same voltage range as the dark curve, but with $n_{ID,rad} = 1$ proving that radiative recombination results from the recombination of an electron in the conduction band with a hole in the valence band. The greater increase of emission current with voltage, compared to overall current, gives rise to an EQE_{EL} (green) that increases with voltage. When plotted as a function of the injection current (Fig. 8b), the EQE_{EL} increases linearly as expected when comparing Eq. 27 with 23 for SRH recombination being dominant.

Having both recombination processes (Eq. 12 and 26) running in parallel, we can write a rate equation assuming that spatial variations in recombination rates and charge carrier densities are negligible, and the majority of the charge carriers are photogenerated:

$$\frac{dn}{dt} = -\beta n^2(t) - \frac{1}{\tau} n(t). \tag{29}$$

This equation can be solved analytically for n as a function of time t , which can be monitored by the emission as a function of t doing a photoluminescence (PL) decay measurement. A varied light intensity of the laser pulse can be used to tune the initial charge carrier density $n(0)$, which allows a more reliable determination of τ and β . Figure 9a shows PL transients including a fit according to the solution of Eq. 29 ($n(t) = \frac{1}{\tau\beta} \frac{1}{e^{\frac{t}{\tau}} \left(\frac{1}{\tau\beta n(0)} + 1 \right) - 1}$), with $\beta \approx 10^{-11} \text{ cm}^3 \text{ s}^{-1}$ and $\tau = 350$ ns.

The value for β coincides with what is expected from the radiative limit, confirming that direct electron-hole recombination is radiative. More sophisticated models including the dynamics of trapping and exciton formation can be applied to fit the

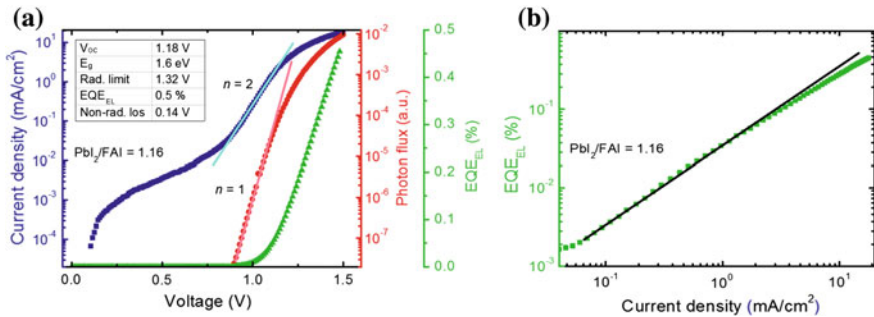


Fig. 8 Highly luminescent perovskite solar cells: **a** Injection current (blue), emitted photon flux (red) and EQE_{EL} as a function of the applied voltage. **b** EQE_{EL} as a function of the injection current. The black line describes a linear relation between EQE_{EL} and the injection current. From [9]. Reprinted with permission from AAAS

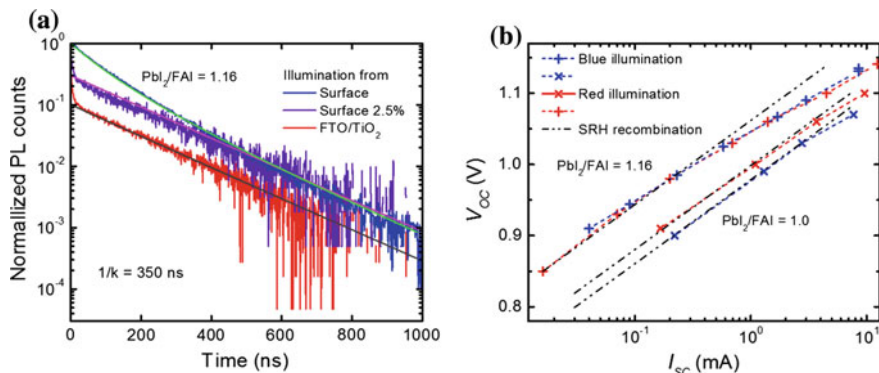


Fig. 9 Optoelectronic characterization of mixed perovskite devices **a** PL decay for illumination from the surface or through the substrate and with high and with 40 times lower light intensity. **b** V_{oc} as a function of illumination intensity under *red* and *blue* light for two different mixed perovskite devices. From [9]. Reprinted with permission from AAAS

PL decay, or other techniques such as transient THz spectroscopy, yielding $\beta \approx 10^{-11} - 10^{-10} \text{cm}^3 \text{s}^{-1}$ [39–41].

The SRH lifetime $\tau \propto \frac{1}{N_T \sigma_T}$ depends on the density (N_T) and capture cross section (σ_T) of electronically active recombination centers. For a charged defect, the latter is inversely proportional to the dielectric constant, which characterizes the ability of the material to screen charge [42]. Thus, the high dielectric constant of $\text{CH}_3\text{NH}_3\text{PbI}_3$ perovskite reported to up to 70 [43] combined with a low N_T for states close to midgap allows for a τ of several 100 s of ns. Here, the role of crystal size, grain boundaries, and passivation agents is not well understood yet [9].

To understand the effect of τ on the solar cell’s performance, we calculate V_{oc} as a function of light intensity for varied τ (Fig. 10). In the radiative limit, V_{oc} increases with light intensity showing a slope of 60 mV/decade (dashed), whereas it shows 120 mV/decade in the case of SRH recombination, which dominates at low light intensity. Investigating V_{oc} at 1 sun (Fig. 10b), we find that a nonradiative lifetime τ of 10 μs would be sufficient to practically reach the radiative limit. The experimental data (symbols) for two perovskite solar cells based on mesoporous TiO_2 are consistent with a τ reaching more than 100 ns.

So far, we have assumed that charge carrier densities and recombination rates in the perovskite film do not depend on the position within the film. However, the direction of incident illumination and vertical inhomogeneities in the morphology of the perovskite layer and different properties at the contacts give rise to lateral inhomogeneities in recombination parameters and charge carrier densities. A treatment of inhomogeneities requires numerical simulations. However, first conclusions can be drawn from qualitative investigations exploiting different inhomogeneities introduced in $G(x)$ by monochromatic illumination. Blue light penetrates the film less than red light, giving rise to a steeper $G(x)$. A modified V_{oc} indicates different charge carrier lifetimes close to the surface and in the bulk.

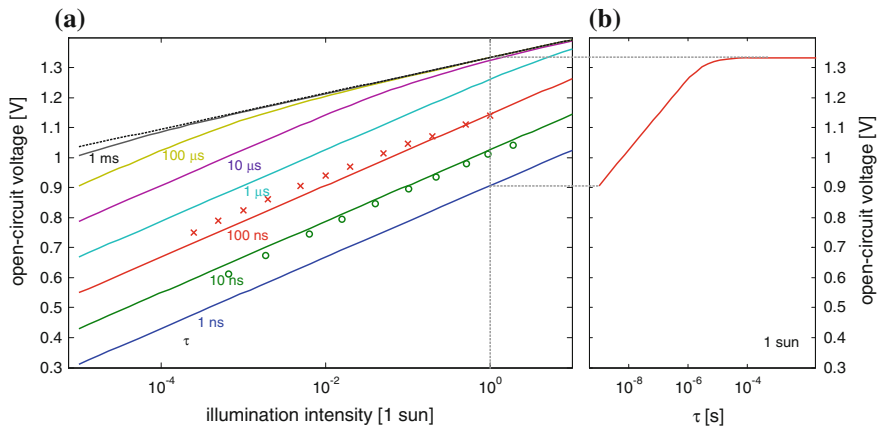


Fig. 10 Calculated influence of the SRH lifetime τ on V_{oc} for a 300 nm thick CH₃NH₃PbI₃ perovskite with a bandgap of 1.6 eV and a radiative recombination constant of 10^{-11} cm³s⁻¹. **a** V_{oc} as a function of illumination intensity and **b** V_{oc} as a function of τ at 1 sun. When SRH recombination is dominant, V_{oc} decreases with 120 mV/decade with illumination intensity and with $1/\tau$. Symbols in **(a)** show experimental data for two-step CH₃NH₃PbI₃ solar cells from Ref. [44] (circles) and for one-step mixed perovskite [45] obtained by a measurement with pulsed light (crosses). Most of the changes in V_{oc} are due to an increased lifetime, as the bandgap changes only by a value <50 meV. A $\tau > 100$ ns is consistent with the PL decay in Fig. 9

The experimental data in Fig. 9b indicates that recombination is stronger at the TiO₂ contact for the device with the lower V_{oc} [9].

Nonradiative recombination influences the fill factor (FF) as well. This can be seen in Eq. 20, where the ideality factor needs to be introduced in front of $k_B T$. In case of negligible series or shunt resistance losses, the FF only depends on recombination. It can be expressed as a function of recombination rate, and thus of V_{oc} . In the radiative limit at 1 sun, it exceeds 90 % (cf. Fig. 4a) and decreases toward 83 % at 1.2 V and 80 % at 1.0 V (Fig. 11). Thus, a perovskite solar cell with a bandgap of 1.6 eV with optimized contacts and a J_{sc} of 24 mA cm⁻², but operating at only 1.0 V cannot deliver a FF greater than 80 %. However, a (slightly) larger FF is possible if recombination does not result from the perovskite itself but from surfaces. This seems to be the case for C₆₀-based electron transport layers [46] in inverted perovskite solar cells, where a FF as high as 85 % is reported for a V_{oc} of 1.03 V [47]. This value requires an $n_{ID} < 2$, when derived from V_{oc} as a function of light intensity. This would be an additional indication for surface recombination limiting V_{oc} [48]. Note that an excessively high FF might result from transient phenomena during measurement, giving rise to hysteresis in the J - V curve [49, 50]. On the other hand, surface recombination can decrease the FF as well. In real solar cells, a low FF is caused by resistive effects due to inhibited charge transport in the absorber or parasitic shunt and series resistances.

The proximity of the FF to the recombination limit (in case of negligible shunting) can be experimentally verified applying the Suns- V_{oc} method [44, 51, 52].

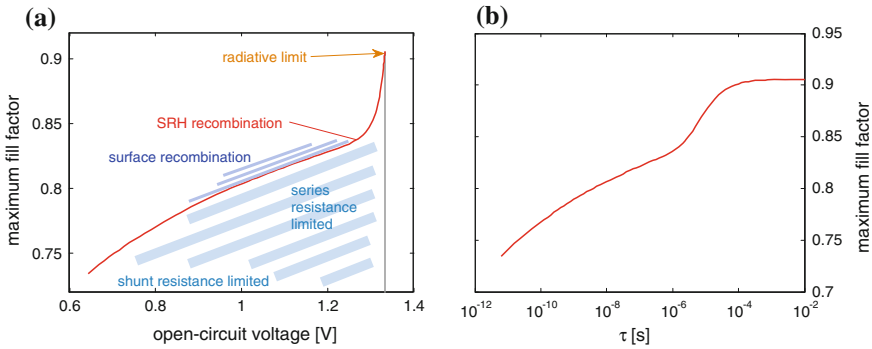


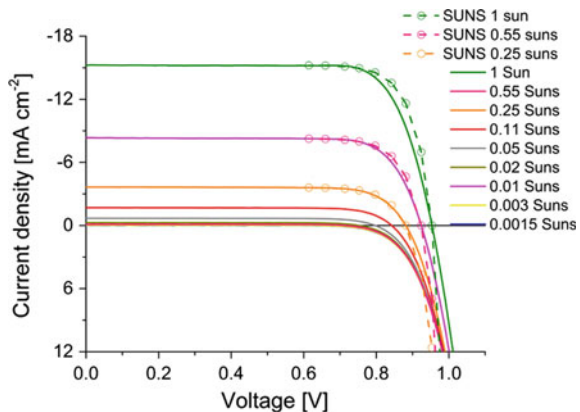
Fig. 11 Calculated fill factor for $\text{CH}_3\text{NH}_3\text{PbI}_3$ perovskite with a bandgap of 1.6 eV and a radiative recombination constant of $10^{-11} \text{ cm}^3\text{s}^{-1}$. **a** The fill factor decreases with lower V_{oc} due to its definition (cf. Fig. 4a). Additionally, a change from the radiation limit to SRH recombination gives rise for the rapid decrease. **b** Fill factor as a function of SRH lifetime τ

Employing this method, a pseudo- J - V curve is constructed from light intensity-dependent V_{oc} data. Series resistance effects are excluded because when measuring V_{oc} , current does not flow. Assuming that the light intensity is proportional to current, the pseudo- J - V curve for a particular intensity I_0 reads:

$$J(V_{\text{oc}}(I)) = J_{\text{sc}}(I_0) \left(1 - \frac{I}{I_0}\right). \quad (30)$$

Figure 12 shows such curves (dashed) for a $\text{CH}_3\text{NH}_3\text{PbI}_3$ perovskite solar cell at different illumination intensities I_0 compared to the measured J - V curves (solid lines) [44]. Both curves coincide at 0.25 suns indicating that charge transport losses in the perovskite are negligible. At higher light intensities and the consequently higher photocurrents, the series resistance limits the FF, mainly due to the resistance of the transparent conductive oxide.

Fig. 12 Current-voltage curves (solid lines) at different illumination intensities. Pseudo- J - V curves (dashed) obtained using the Suns- V_{oc} method. Reprinted with permission from [44]. Copyright 2015 American Chemical Society



3.3 Role of the Charge Transport Layers

In the theoretical discussions, we assumed that contacts were perfect. Through experiments, we have already seen that they can change EQE_{EL} and thus be a source of nonradiative recombination, e.g., if a hole transport layer (HTL) is not used (cf. Table 1).

Thus, an essential role of the charge transport layers is to provide a selective contact. The electron transport layer (ETL) should only allow electrons to pass and block holes, and the HTL vice versa. This property can be put into practice by a large energy barrier for electron (hole) transfer due to offsets in conduction (valence) band. Additionally, recombination at the interface between the absorber and the charge transport layer should be avoided. This type of recombination, where charge recombines at the surface of the absorber, is called surface recombination and it is characterized by a surface recombination velocity. For metals, the surface recombination velocity is usually very high for both electrons and holes. Hence, metals are not a good choice for selective contacts.

In general, interfaces between two materials (heterojunctions) might fulfill the role of separation of charge or excited states, as in the case of organic donor–acceptor heterojunctions [2]. However, from the previous discussions, there are no indications that interfaces are essential for the photovoltaic working principle of perovskite solar cells. Thus, charges are generated and dissociated in the perovskite itself, creating a splitting of the quasi-Fermi levels, which gives rise to the photovoltage. The charge transport layers just serve as contacts. However, this raises the question on the operational principle of perovskite solar cells, where no intentional pn junction is introduced, in contrast to conventional solar cells. From the discussions above, we know that a pn junction itself is not a requirement for a solar cell. Instead, selective contacts are sufficient. The solar cell architecture comprises of a metal–insulator (semiconductor)–metal structure. Charges can be driven toward their respective interface simply by diffusion. Usually, a difference in work function of the two metals (or transparent conductive oxides) is beneficial, though not required, as it introduces a built-in potential similar to the different types of doping in a pn junction. To date it is not clear whether the assumption of a constant electric field in the perovskite is justified. Space charge regions could result from unintentional doping, the existence of mobile ionic species, grain boundaries, or other inhomogeneities in the film.

A lot of research focuses on interchanging ETL or HTL to increase performance and in particular V_{oc} . Regarding the ETL, high $V_{\text{oc}} > 1\text{V}$ has been obtained with several materials such as TiO_2 with TiO_2 or Al_2O_3 scaffold [6], PCBM [53], ZnO [54], or $\text{Ti}(\text{Nb})\text{O}_x$ [55]. Record values of 1.2 V have been achieved with TiO_2 [9] and SnO_2 [56], where the high V_{oc} is mainly attributed to an improved morphology of the perovskite. One approach commonly taken up is the tuning of the HOMO level of the organic HTL. It is anticipated that a lower lying HOMO increases V_{oc} . The experimental effort on testing HTLs to increase V_{oc} has only been partly successful [57–59] but clear trends are mostly missing [60–64]. Instead,

improvements of V_{oc} were obtained by modifying the perovskite [9]. This is expected from the discussion in this chapter. Modifying the HTL or ETL to increase V_{oc} is only important if recombination at the HTL(Au)/perovskite interface reduces V_{oc} (possibly independent of HOMO position), as it is the case for, e.g., too thin HTL [44] or PEDOT:PSS as HTL [65]. A deeper lying HOMO accompanied by a higher work function of a doped HTL could increase the built-in potential and thus reduce surface recombination as less charges are reaching the wrong electrode. However, if the surface is well passivated, i.e., recombination at the electrode is not an issue, changes in the HOMO of the HTL will not affect V_{oc} . In addition, the formation of interface dipoles can change band alignment compared to the case predicted by assuming a constant vacuum level at the interface.

Theoretically, V_{oc} can exceed the difference between the work functions of the contacts or the difference between the conduction and the valence band of electron and hole transport layer, respectively. This is thought to be counter intuitive, but with restrictions this is as normal as the fact that it is possible to apply a voltage larger than those offsets. The results for Br-based perovskite on TiO_2 and HTL spiro-OMeTAD with V_{oc} approaching 1.5 V indicate that this is possible in experiment as well [66]. Thus, it is more important to tune the HTL and ETL to reduce recombination centers on their surfaces, which might result from additives, and use the charge transport layers to passivate the perovskite surface instead of solely focusing on the energetics.

Acknowledgments I thank Amita Ummadisingu for carefully reading the text and suggesting improvements regarding language. Marko Stojanovic, Juan Pablo Correa Baena, T. Jesper Jacobsson, Yiming Cao, and Somayyeh Gholipour are acknowledged for commenting on the manuscript. I thank Dongqin Bi for providing I:Br samples, and Clémentine Renevier and Björn Niessen for the collaboration regarding the characterization of those samples. Financial support from SNF-NanoTera (SYNERGY) is kindly acknowledged.

References

1. Würfel, P.: *Physics of Solar Cells: From Basic Principles to Advanced Concepts*. (Wiley)
2. Tress, W.: *Organic Solar Cells—Theory, Experiment, and Device Simulation*
3. Trupke, T., Daub, E., Würfel, P.: Absorptivity of silicon solar cells obtained from luminescence. *Sol. Energy Mater. Sol. Cells* **53**, 103–114 (1998)
4. Rau, U.: Reciprocity relation between photovoltaic quantum efficiency and electroluminescent emission of solar cells. *Phys. Rev. B* **76**, 085303 (2007)
5. Giorgi, G., Fujisawa, J.-I., Segawa, H., Yamashita, K.: Small photocarrier effective masses featuring ambipolar transport in methylammonium lead iodide perovskite: a density functional analysis. *J. Phys. Chem. Lett.* **4**, 4213–4216 (2013)
6. Tress, W., et al.: Predicting the open-circuit voltage of $CH_3NH_3PbI_3$ perovskite solar cells using electroluminescence and photovoltaic quantum efficiency spectra: the role of radiative and non-radiative recombination. *Adv. Energy Mater.* **5**, 140812 (2015)
7. Tvingstedt, K., et al.: Radiative efficiency of lead iodide based perovskite solar cells. *Sci. Rep.* **4**, 6071 (2014)

8. Ball, J.M., et al.: Optical properties and limiting photocurrent of thin-film perovskite solar cells. *Energy Environ. Sci.* **8**, 602–609 (2015)
9. Bi, D., et al.: Efficient luminescent solar cells based on tailored mixed-cation perovskites. *Sci. Adv.* **2**, e1501170 (2016)
10. Shockley, W., Queisser, H.J.: Detailed balance limit of efficiency of p-n junction solar cells. *J. Appl. Phys.* **32**, 510–519 (2004)
11. Green, M.A., Emery, K., Hishikawa, Y., Warta, W., Dunlop, E.D.: Solar cell efficiency tables (version 46). *Prog. Photovolt. Res. Appl.* **23**, 805–812 (2015)
12. De Wolf, S., et al.: Organometallic halide perovskites: sharp optical absorption edge and its relation to photovoltaic performance. *J. Phys. Chem. Lett.* **5**, 1035–1039 (2014)
13. D’Innocenzo, V., Srimath Kandada, A.R., De Bastiani, M., Gandini, M., Petrozza, A.: Tuning the light emission properties by band gap engineering in hybrid lead halide perovskite. *J. Am. Chem. Soc.* **136**, 17730–17733 (2014)
14. Stoumpos, C.C., Malliakas, C.D., Kanatzidis, M.G.: Semiconducting tin and lead iodide perovskites with organic cations: phase transitions, high mobilities, and near-infrared photoluminescent properties. *Inorg. Chem.* **52**, 9019–9038 (2013)
15. Pang, S., et al.: NH₂CH=NH₂PbI₃: an alternative organolead iodide perovskite sensitizer for mesoscopic solar cells. *Chem. Mater.* **26**, 1485–1491 (2014)
16. Pellet, N., et al.: Mixed-organic-cation perovskite photovoltaics for enhanced solar-light harvesting. *Angew. Chem. Int. Ed.* **53**, 3151–3157 (2014)
17. Eperon, G.E., et al.: Formamidinium lead trihalide: a broadly tunable perovskite for efficient planar heterojunction solar cells. *Energy Environ. Sci.* **7**, 982–988 (2014)
18. Filip, M.R., Eperon, G.E., Snaith, H.J., Giustino, F.: Steric engineering of metal-halide perovskites with tunable optical band gaps. *Nat. Commun.* **5**, (2014)
19. Amat, A., et al.: Cation-induced band-gap tuning in organohalide perovskites: interplay of spin-orbit coupling and octahedra tilting. *Nano Lett.* **14**, 3608–3616 (2014)
20. Umebayashi, T., Asai, K., Kondo, T., Nakao, A.: Electronic structures of lead iodide based low-dimensional crystals. *Phys. Rev. B* **67**, 155405 (2003)
21. Noh, J.H., Im, S.H., Heo, J.H., Mandal, T.N., Seok, S.I.: Chemical management for colorful, efficient, and stable inorganic-organic hybrid nanostructured solar cells. *Nano Lett.* **13**, 1764–1769 (2013)
22. McMeekin, D.P., et al.: A mixed-cation lead mixed-halide perovskite absorber for tandem solar cells. *Science* **351**, 151–155 (2016)
23. Henry, C.H.: Limiting efficiencies of ideal single and multiple energy gap terrestrial solar cells. *J. Appl. Phys.* **51**, 4494–4500 (1980)
24. Albrecht, S., et al.: Monolithic perovskite/silicon-heterojunction tandem solar cells processed at low temperature. *Energy Environ. Sci.* (2015). doi:[10.1039/C5EE02965A](https://doi.org/10.1039/C5EE02965A)
25. Werner, J., et al.: Efficient monolithic perovskite/silicon tandem solar cell with cell area >1 cm². *J. Phys. Chem. Lett.* **7**, 161–166 (2016)
26. Mailoa, J.P., et al.: A 2-terminal perovskite/silicon multijunction solar cell enabled by a silicon tunnel junction. *Appl. Phys. Lett.* **106**, 121105 (2015)
27. Löper, P., et al.: Organic–inorganic halide perovskite/crystalline silicon four-terminal tandem solar cells. *Phys. Chem. Chem. Phys.* **17**, 1619–1629 (2014)
28. Filipič, M., et al.: CH₃NH₃PbI₃ perovskite/silicon tandem solar cells: characterization based optical simulations. *Opt. Express* **23**, A263 (2015)
29. Smestad, G., Ries, H.: Luminescence and current-voltage characteristics of solar cells and optoelectronic devices. *Sol. Energy Mater. Sol. Cells* **25**, 51–71 (1992)
30. Burschka, J., et al.: Sequential deposition as a route to high-performance perovskite-sensitized solar cells. *Nature* **499**, 316–319 (2013)
31. Yao, J., et al.: Quantifying losses in open-circuit voltage in solution-processable solar cells. *Phys. Rev. Appl.* **4**, 014020 (2015)
32. Tiedje, T., Yablonovitch, E., Cody, G.D., Brooks, B.G.: Limiting efficiency of silicon solar cells. *IEEE Trans. Electron Devices* **31**, 711–716 (1984)

33. Kerr, M.J., Cuevas, A., Campbell, P.: Limiting efficiency of crystalline silicon solar cells due to Coulomb-enhanced Auger recombination. *Prog. Photovolt. Res. Appl.* **11**, 97–104 (2003)
34. Kim, J., Lee, S.-H., Lee, J.H., Hong, K.-H.: The Role of Intrinsic Defects in Methylammonium Lead Iodide Perovskite. *J. Phys. Chem. Lett.* 1312–1317 (2014). doi:[10.1021/jz500370k](https://doi.org/10.1021/jz500370k)
35. Yin, W.-J., Shi, T., Yan, Y.: Unusual defect physics in CH₃NH₃PbI₃ perovskite solar cell absorber. *Appl. Phys. Lett.* **104**, 063903 (2014)
36. Buin, A., et al.: Materials processing routes to trap-free halide perovskites. *Nano Lett.* **14**, 6281–6286 (2014)
37. Agiorgousis, M.L., Sun, Y.-Y., Zeng, H., Zhang, S.: Strong Covalency-Induced Recombination Centers in Perovskite Solar Cell Material CH₃NH₃PbI₃. *J. Am. Chem. Soc.* **136**, 14570–14575 (2014)
38. Shockley, W., Read, W.T.: Statistics of the recombinations of holes and electrons. *Phys. Rev.* **87**, 835–842 (1952)
39. Wehrenfennig, C., Eperon, G.E., Johnston, M.B., Snaith, H.J., Herz, L.M.: High charge carrier mobilities and lifetimes in organolead trihalide perovskites. *Adv. Mater.* **26**, 1584–1589 (2014)
40. Stranks, S.D., et al.: Recombination kinetics in organic-inorganic perovskites: excitons, free charge, and subgap states. *Phys. Rev. Appl.* **2**, 034007 (2014)
41. Yamada, Y., Nakamura, T., Endo, M., Wakamiya, A., Kanemitsu, Y.: Photocarrier Recombination Dynamics in Perovskite CH₃NH₃PbI₃ for Solar Cell Applications. *J. Am. Chem. Soc.* **136**, 11610–11613 (2014)
42. Brandt, R.E., Stevanović, V., Ginley, D.S., Buonassisi, T.: Identifying defect-tolerant semiconductors with high minority-carrier lifetimes: beyond hybrid lead halide perovskites. *MRS Commun.* **5**, 265–275 (2015)
43. Lin, Q., Armin, A., Nagiri, R.C.R., Burn, P.L., Meredith, P.: Electro-optics of perovskite solar cells. *Nat. Photonics* (advance online publication), (2014)
44. Marinova, N., et al.: Light harvesting and charge recombination in CH₃NH₃PbI₃ perovskite solar cells studied by hole transport layer thickness variation. *ACS Nano* (2015). doi:[10.1021/acsnano.5b00447](https://doi.org/10.1021/acsnano.5b00447)
45. Giordano, F., et al.: Enhanced electronic properties in mesoporous TiO₂ via lithium doping for high-efficiency perovskite solar cells. *Nat. Commun.* **7**, 10379 (2016)
46. Ponseca, C.S., et al.: Mechanism of charge transfer and recombination dynamics in organo metal halide perovskites and organic electrodes, PCBM, and spiro-OMeTAD: role of dark carriers. *J. Am. Chem. Soc.* **137**, 16043–16048 (2015)
47. Wu, C.-G., et al.: High efficiency stable inverted perovskite solar cells without current hysteresis. *Energy Environ. Sci.* **8**, 2725–2733 (2015)
48. Tress, W., Leo, K., Riede, M.: Dominating recombination mechanisms in organic solar cells based on ZnPc and C60. *Appl. Phys. Lett.* **102**, 163901 (2013)
49. Snaith, H.J., et al.: Anomalous hysteresis in perovskite solar cells. *J. Phys. Chem. Lett.* **5**, 1511–1515 (2014)
50. Tress, W., et al.: Understanding the rate-dependent J-V hysteresis, slow time component, and aging in CH₃NH₃PbI₃ perovskite solar cells: the role of a compensated electric field. *Energy Environ. Sci.* **8**, 995–1004 (2015)
51. Pysch, D., Mette, A., Glunz, S.W.: A review and comparison of different methods to determine the series resistance of solar cells. *Sol. Energy Mater. Sol. Cells* **91**, 1698–1706 (2007)
52. Schiefer, S., Zimmermann, B., Glunz, S.W., Würfel, U.: Applicability of the suns-V method on organic solar cells. *IEEE J. Photovolt.* **4**, 271–277 (2014)
53. Malinkiewicz, O., et al.: Perovskite solar cells employing organic charge-transport layers. *Nat. Photonics* **8**, 128–132 (2014)
54. Liu, D., Kelly, T.L.: Perovskite solar cells with a planar heterojunction structure prepared using room-temperature solution processing techniques. *Nat. Photonics* **8**, 133–138 (2014)
55. Chen, W., et al.: Efficient and stable large-area perovskite solar cells with inorganic charge extraction layers. *Science* **350**, 944–948 (2015)

56. Baena, J.P.C., et al.: Highly efficient planar perovskite solar cells through band alignment engineering. *Energy Environ. Sci.* (2015). doi:[10.1039/C5EE02608C](https://doi.org/10.1039/C5EE02608C)
57. Heo, J.H., Song, D.H., Im, S.H.: Planar CH₃NH₃PbBr₃ hybrid solar cells with 10.4 % power conversion efficiency, fabricated by controlled crystallization in the spin-coating process. *Adv. Mater.* n/a–n/a (2014). doi:[10.1002/adma.201403140](https://doi.org/10.1002/adma.201403140)
58. Yan, W., et al.: High-performance hybrid perovskite solar cells with open circuit voltage dependence on hole-transporting materials. *Nano Energy*. doi:[10.1016/j.nanoen.2015.07.024](https://doi.org/10.1016/j.nanoen.2015.07.024)
59. Ryu, S., et al.: Voltage output of efficient perovskite solar cells with high open-circuit voltage and fill factor. *Energy Environ. Sci.* (2014). doi:[10.1039/C4EE00762J](https://doi.org/10.1039/C4EE00762J)
60. Liu, J., et al.: A dopant-free hole-transporting material for efficient and stable perovskite solar cells. *Energy Environ. Sci.* **7**, 2963–2967 (2014)
61. Polander, L.E., et al.: Hole-transport material variation in fully vacuum deposited perovskite solar cells. *APL Mater.* **2**, 081503 (2014)
62. Di Giacomo, F., et al.: High efficiency CH₃NH₃PbI(3–x)Cl_x perovskite solar cells with poly(3-hexylthiophene) hole transport layer. *J. Power Sources* **251**, 152–156 (2014)
63. Bi, D., Yang, L., Boschloo, G., Hagfeldt, A., Johansson, E.M.J.: Effect of different hole transport materials on recombination in CH₃NH₃PbI₃ perovskite-sensitized mesoscopic solar cells. *J. Phys. Chem. Lett.* **4**, 1532–1536 (2013)
64. Jeon, N.J., et al.: Efficient inorganic-organic hybrid perovskite solar cells based on pyrene arylamine derivatives as hole-transporting materials. *J. Am. Chem. Soc.* **135**, 19087–19090 (2013)
65. Zhao, D., et al.: High-efficiency solution-processed planar perovskite solar cells with a polymer hole transport layer. *Adv. Energy Mater.* **5**, n/a–n/a (2015)
66. Arora, N., Dar, M.I., Hezam, M., Tress, W., Jacopin, G., Moehl, T., Gao, P., Aldwayyan, A.S., Benoit, D., Grätzel, M., Nazeeruddin, M.K.: Photovoltaic and amplified spontaneous emission studies of high-quality formamidinium lead bromide perovskite films. *Adv. Func. Mat.*